Particuology 115 (2026) 25–34

Contents lists available at ScienceDirect

Particuology

journal homepage: www.elsevier.com/locate/partic

Hydrogen-free cyclized polyacrylonitrile binder enables thermally robust lithium-ion batteries

Kai Chen[a], Dian Zhang[a], Feng Jiang[a], Nai-Lu Shen[a], Xiao-Hui Yan[a], Ke-Feng Ren[b], Xin Shen[a,*], Lungang Chen[c], He Liu[b,**], Faxing Wang[a], Shengjie Peng[a], Yuping Wu[a], Xin-Bing Cheng[a,***]

[a] Z Energy Storage Center, School of Energy and Environment, Southeast University, Nanjing, 211189, China
[b] Jiangsu Key Laboratory of New Energy Devices & Interface Science, School of Chemistry and Materials Science, Nanjing University of Information Science and Technology, Nanjing, 210044, China
[c] Key Laboratory of Energy Thermal Conversion and Control of Ministry of Education, School of Energy and Environment, Southeast University, Nanjing, 211189, China

HIGHLIGHTS

- Cyclized polyacrylonitrile binder can inhibit the generation of hydrogen.
- Cyclized polyacrylonitrile binder serves as a lithium-ion storage material.
- Cyclized polyacrylonitrile binder suppresses side reactions of the electrolyte.

GRAPHICAL ABSTRACT

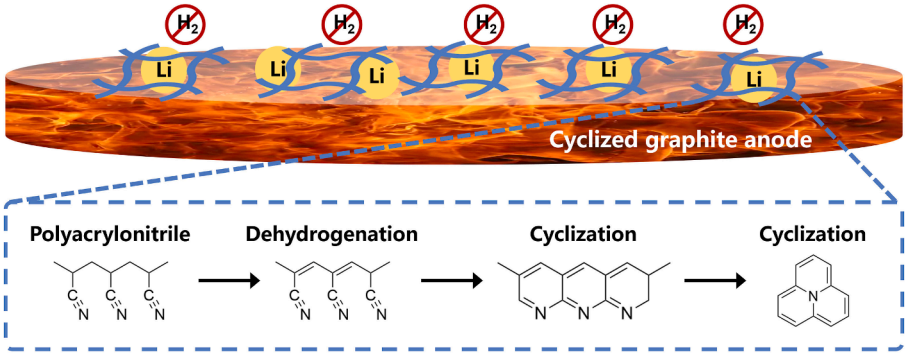

ARTICLE INFO

Keywords:
Lithium-ion battery
Thermal runaway
Hydrogen
Binder
Cyclized polyacrylonitrile

ABSTRACT

Hydrogen generation during thermal runaway significantly elevates the risk of explosive combustion in lithium-ion batteries. Although hydrogen generated from binders constitutes a minor fraction, its absolute quantity remains substantial in large-scale stationary energy storage systems. Moreover, binder decomposition occurs during the later stages of thermal runaway with rapid reaction rates, further raising the danger level. Herein, graphite anode with polyacrylonitrile binder is *in situ* cyclized to eliminate the active hydrogen, while maintaining superior cohesiveness. On one hand, cyclized polyacrylonitrile with largely reduced hydrogen atoms can prevent binder-induced hydrogen generation and realize a reduction of hydrogen fraction by over 23%. As the three-dimensional cross-linking binders increase the thermal stability of anodes, the peak decomposition temperature of solid electrolyte interphase is increased from 150 to 200 °C to above 200 °C, while the peak reaction temperature between lithiated graphite and the electrolyte is delayed by at least 15 °C. On the other hand, the

This article is part of a special issue entitled: SI honoring Profs. Jin & Yu published in Particuology.

* Corresponding author.
** Corresponding author.
*** Corresponding author.
E-mail addresses: shenx25@seu.edu.cn (X. Shen), liuhe@nuist.edu.cn (H. Liu), chengxb@seu.edu.cn (X.-B. Cheng).

https://doi.org/10.1016/j.partic.2026.05.005
Received 15 April 2026; Received in revised form 8 May 2026; Accepted 9 May 2026
Available online 16 May 2026

transformation from linear to cyclic molecular structures of cyclized polyacrylonitrile enables uniform and tight encapsulation of graphite and enhanced cohesiveness. Capacity retentions of 97% after 200 cycles in half cells and 72% after 800 cycles in full cells are achieved.

1. Introduction

The development of sustainable energy sources has become increasingly important to handle the growing concerns over the excessive consumption of fossil energy (Luo et al., 2025; Zantye et al., 2022; Zhang, Li, et al., 2018). However, sustainable energies such as solar and wind power are inherently intermittent and volatile, posing an urgent demand for energy storage technology (Guerra et al., 2020). To ensure long-term, stable, and universal access to sustainable energy, electrochemical energy storage offers an effective solution (Chen et al., 2026; Ding et al., 2025; Jiang et al., 2025; Seong et al., 2018). Lithium-ion batteries (LIBs), particularly lithium iron phosphate (LFP) batteries, have gained widespread application in electrochemical energy storage due to their long cycle life, high safety, and low cost (Jiang et al., 2023; Luo et al., 2024; Wang et al., 2022). This makes LFP LIBs among the most promising electrochemical systems for large-scale energy storage applications (Lei et al., 2024; Yu et al., 2025).

With the advancement of large-scale energy storage applications, it is imperative to address the safety concerns associated with large-capacity lithium-ion batteries (Bashir et al., 2025; Jiang, Wen, et al., 2024; Meng et al., 2022). Under conditions of external abuse, lithium-ion batteries are prone to thermal runaway, which can lead to explosive combustion (Feng et al., 2020; Guo et al., 2025; Jiang, Luo, et al., 2025). LFP crystals possess an olivine-type structure, which confers excellent structural stability (Chen et al., 2025; Yang et al., 2021; Zhao et al., 2024). During the thermal runaway, compared to nickel-cobalt-manganese LIBs, LFP LIBs exhibit a higher triggering temperature, as well as lower maximum temperature, temperature rising rate, accumulated heat, mass loss and combustion possibility (Huang et al., 2021; Shi et al., 2026; Wang et al., 2021). Therefore, LFP LIBs, which are relatively safer among commonly used LIBs, represent the optimal choice for large-scale energy storage applications. However, in recent years, safety incidents involving LFP LIBs in large-scale energy storage applications frequently occur, even leading to some casualties (Wang, Xu, et al., 2022; Zhang et al., 2026). It is found that the gases released during thermal runaway of LFP LIBs contain a significant proportion of flammable and explosive components, among which hydrogen (H_2) poses the greatest hazard due to its low flammability limit and high concentration (Shen et al., 2023; Wei et al., 2023).

The primary sources of H_2 in the thermal runaway gases include the decomposition of trace water, reduction of the electrolyte, reduction of hydrofluoric acid and decomposition of the binder (Kim et al., 2020; Metzger et al., 2016; Zheng et al., 2022). Given its low concentration, the impact of H_2 generation from trace water is relatively minor. The H_2 generated from electrolyte and hydrofluoric acid is extensively investigated and can be mitigated by regulating electrolyte composition and improving the solid electrolyte interphase (SEI) (Jiang et al., 2024). However, studies focusing on the thermal safety of binders remain limited. At elevated temperatures, the binder reacts with lithium to generate H_2. Although the binder accounts for a minor mass fraction in the electrode, its decomposition-induced H_2 generation occurs during the mid-to-late stages of thermal runaway (Liu et al., 2021). At this phase, the rate of temperature rise is significantly high, rendering subsequent measures to suppress H_2 generation largely ineffective. Moreover, in large-scale energy storage applications, the absolute quantity of binder is considerable, resulting in a non-negligible amount of H_2 generation. Therefore, the thermal safety of binders warrants significant attention. Commonly used binders such as poly (vinylidene fluoride) (PVDF) and sodium carboxymethylcellulose have been reported to decompose and generate H_2 (Chen, Zhang, et al., 2025; Jia et al., 2022; Liu et al., 2021). Polytetrafluoroethylene binder does not generate H_2 due to the absence of hydrogen atoms in its molecular structure. However, limited cohesiveness of polytetrafluoroethylene hinders its practical application as a binder (Qin et al., 2024). Consequently, developing binders that do not generate H_2 while maintain superior cohesiveness is of critical importance for the safe operations of long-lifespan lithium-ion batteries.

In this study, the graphite anode of LIBs is directly heated to induce the cyclization of the polyacrylonitrile (PAN) binder, forming *in situ* cyclized polyacrylonitrile (cPAN) with a stable cyclic molecular structure. Commonly used binders such as PVDF react with lithium during thermal runaway, where C–H bond cleavage leads to the generation of hazardous H_2 (Fig. 1(a)). In contrast, cPAN maintains structural stability throughout the thermal runaway, remains unaffected by lithium, and exhibits thermally safe characteristics by preventing H_2 generation (Fig. 1(b)). Furthermore, compared to linear PAN, cPAN possesses a crosslinked network structure that distributes more uniformly and densely on the graphite (Gr) surface. This process enables cPAN to better encapsulate Gr and reinforces the SEI, which inhibits electron transfer to the electrolyte and hydrofluoric acid, thus reducing H_2 generation. Besides, cPAN can serve as an active material for lithium storage, demonstrating a high reversible capacity of up to 1238 mAh g^{-1} at a current density of 50 mA g^{-1} (Zhang et al., 2021). Owing to the increased lithium storage active sites, electrodes possess reduced charge transfer resistance. Consequently, electrodes containing cPAN display excellent electrochemical performance.

2. Results and discussion

2.1. Cyclization from PAN to cPAN

A significant weight loss and an exothermic peak at 291 °C indicates the transformation of linear PAN into crosslinked cPAN by thermogravimetric analysis (TG) and differential scanning calorimetry (DSC) of PAN powder (see Supplementary Fig. S1). To ensure the complete transformation of PAN to cPAN, the cyclization condition is set at 300 °C for 12 h. PAN initially undergoes dehydrogenation, forming C=C bonds, followed by cyclization, during which the characteristic C ≡ N bonds disappear while C–N and C=N bonds are formed. Ultimately, under sustained heating at 300 °C, PAN is fully cyclized into a crosslinked network structure (Fig. 2(a)) (Hong et al., 2025). During this high-temperature treatment, the color of PAN changes from white to brown, consistent with previous researches, confirming the successful synthesis of cPAN (Fig. 2(b)) (Zhang et al., 2021).

Two characteristic peaks at 2245 and 1450 cm^{-1}, attributed to C ≡ N and CH_2 bonds respectively, are observed in the Fourier transform infrared spectroscopy (FTIR) spectra of PAN (Fig. 2(c)) (Sun et al., 2021; Zhang et al., 2018). During cyclization, dehydrogenation leads to the disappearance of CH_2 bonds, while the C ≡ N undergoes transformation into C–N and C=N bonds. These molecular structural changes are confirmed by the absence of C ≡ N and CH_2 peaks in the FTIR spectrum of cPAN, alongside new characteristic peaks at 1257 and 1596 cm^{-1} corresponding to C–N and C=N or C=C bonds, indicating successful cyclization (Chiu et al., 2025; Zhang et al., 2021). The structural transformation of PAN during cyclization is further corroborated by X-ray diffraction (XRD) patterns. A prominent peak at 17°, corresponding to the (100) planes of the hexagonal structure of PAN, disappears after thermal treatment, while a new peak emerges at 25.5°, attributable to the (002) planes of a pre-graphitic structure, signifying the formation of the cyclic structure (Fig. 2(d)) (Sun et al., 2021). No

distinct characteristic peaks are observed in the Raman spectrum of PAN (Fig. 2(e)). In contrast, cPAN displays typical disordered (D) and graphitic (G) peaks at 1360 and 1570 cm^{-1}, respectively, indicating the coexistence of sp^3 hybridized C–C (C–N) and sp^2 hybridized C=C (C=N) structures (Zhang et al., 2021). Collectively, the changes in color, FTIR spectra, XRD patterns, and Raman spectra conclusively demonstrate that the thermal treatment applied in this study successfully converts PAN into cPAN.

2.2. The cPAN binders in anode

In this study, direct heating of the electrodes is employed to induce *in situ* cyclization of PAN binders, resulting in the formation of cPAN in the Gr anode (Fig. 3(a)). After thermal treatment, no discernible changes are observed in optical photographs of the electrodes, indicating that only the PAN binders undergo cyclization. The distribution of binders on the Gr surface is investigated by scanning electron microscopy (SEM) and high-resolution transmission electron microscopy (HRTEM) (Fig. 3(b–e) and S2). Both PAN- and PVDF-based electrodes display exposed Gr regions with non-uniform binder distribution across the Gr particle surfaces. cPAN provides a dense and uniform coverage of the Gr surface, forming a protective physical barrier that suppresses electrolyte side reactions at the Gr electrode. This effect is critical for endowing electrodes with superior thermal safety, mechanical integrity, and electrochemical performance. XRD analysis is conducted to examine the phase structure of Gr electrodes prepared with three different binders: PVDF, PAN and cPAN (Fig. 3(f)). The diffraction peaks of all three electrodes corresponded well with Gr, demonstrating that the Gr crystal structure remains unaffected by the thermal treatment (Agostini et al., 2016; Lavi et al., 2019; Zhang et al., 2025). Differences observed in the Raman spectra among the three electrodes confirm that the electrode with cPAN binder undergoes a higher level of cyclization after heat treatment (Fig. 3(g)). All electrodes possess distinct D and G peaks. However, the intensity ratio of the D to the G peaks (I_D/I_G) for the cPAN-based electrode is significantly higher than those of the other electrodes, indicating a more disordered microstructure (Piper et al., 2013; Wang et al., 2016; Xu et al., 2024).

To evaluate the mechanical performance of cPAN after thermal treatment, folding tests are performed on the electrodes. The cPAN-based electrode demonstrates excellent mechanical performance, with no significant loss of mass after repeated folding and unfolding cycles, suggesting that cPAN is conducive to stable cycling (Fig. 3(h) and S3). Adhesion tests using adhesive tape further compare the mechanical performance. Electrodes with PVDF and PAN binders lose substantial active material upon tape peeling. The cPAN-based electrode shows negligible material detachment, indicating that the crosslinked molecular network of cPAN effectively protects the active material and provides superior adhesion properties (Fig. 3(i)). The adhesion strength between the active material and the current collector is further evaluated using the 180° peeling test (Fig. S4). The cPAN-based electrode shows a maximum peeling force of 2.36 N, whereas the PVDF- and PAN-based electrodes exhibit values below 0.5 N. After peeling, a larger amount of active material remains adhered to the surface of the cPAN-based electrode compared with the other two electrodes. These results demonstrate that cPAN provides stronger adhesion between the active material and the current collector, thereby exhibiting superior mechanical performance. Moreover, the contact angle of electrolyte on cPAN-based electrodes is significantly smaller than those on electrodes with PVDF and PAN binders. This suggests enhanced interaction between the electrolyte and the cPAN binder, facilitating improved electrolyte infiltration and wetting of the electrode (Fig. 3(j)). Consequently, the *in situ* cyclization process does not compromise the intrinsic Gr structure but notably enhances the mechanical properties of the electrodes.

2.3. Thermal safety

Improving the safety performance of LFP LIBs fundamentally hinges on reducing the flammability of the thermal runaway gas. This is realized by employing cPAN to suppress H_2 generation, ultimately decreasing H_2 fraction. To evaluate the capability of cPAN in suppressing H_2 generation, ten identical coin cells are placed in a sealed reaction kettle and subjected to thermal runaway (Fig. S5). The gases generated during thermal runaway are subsequently collected and analyzed for H_2 fraction (Fig. 4(a)). The thermal runaway gases of LIBs employing PVDF and PAN binders contain 0.81% and 0.97% hydrogen, respectively. The hydrogen fraction in the thermal runaway gases of LIBs using cPAN binder is significantly reduced to 0.62%, representing a reduction of at least 23% compared to the others (Fig. 4(b) and S6). H_2 generation originates from trace water decomposition, electrolyte reduction, hydrofluoric acid reduction, and binder decomposition. However, since the binder serves as the sole variable, the reduction in

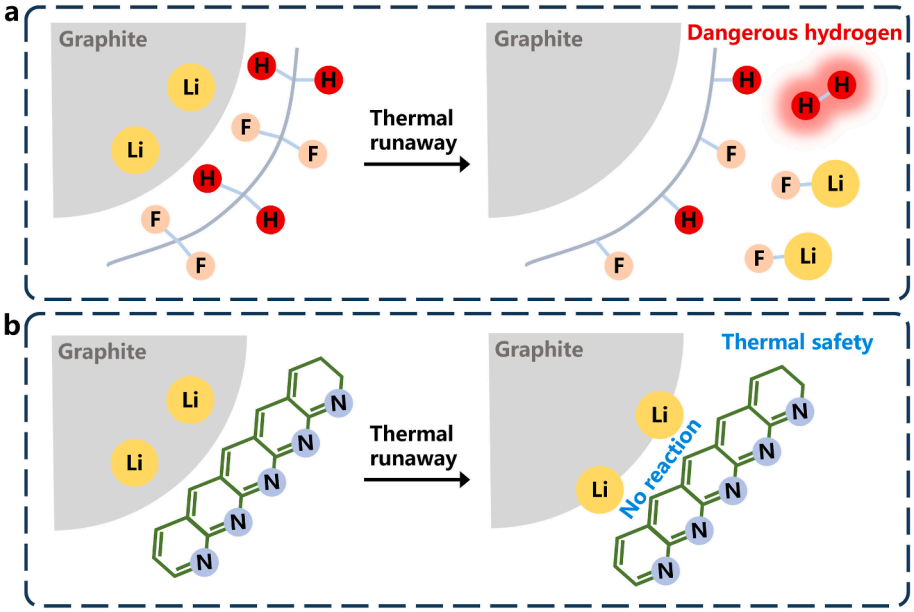

Fig. 1. Diagram of H_2 generation from (a) PVDF and (b) cPAN.

the H_2 fraction is attributable to the excellent thermal stability of cPAN, which prevents its decomposition and subsequent H_2 generation. In addition to acute thermal runaway, cPAN-based LIBs maintain a H_2 fraction of 0.6–0.7% under chronic thermal stress, which remains lower than that of PVDF- and PAN-based LIBs, thereby confirming the superior thermal stability of cPAN (Fig. S7). Furthermore, cPAN forms a physical barrier on the Gr surface, reducing direct contact between the electrolyte and lithiated Gr. This barrier also prevents the electrolyte and hydrofluoric acid from gaining electrons at the anode surface, thereby suppressing their reduction and the consequent generation of H_2.

To further substantiate the multi-dimensional H_2 suppression effect of cPAN, differential scanning calorimetry (DSC) tests are conducted on lithiated Gr electrodes prepared under different conditions. Three Gr electrodes are lithiated to the same capacity. In the absence of electrolyte, the DSC curves of all three samples display two exothermic peaks (Fig. 4(c)). The first peak corresponds to the decomposition of SEI, while the second is attributed to the reaction between the binder and lithium (Guo et al., 2024; Ren et al., 2021; Zhang et al., 2023). Compared with cPAN-based electrode, where an exothermic peak occurs above 200 °C, lithiated Gr electrodes with PVDF and PAN binders undergo SEI decomposition and release significant heat in the range of 150–200 °C, indicating poorer cycling stability. This instability leads to continuous SEI rupture and reformation, generating a large quantity of organic products. In contrast, cPAN-based electrodes form a uniform coating on Gr surfaces, reducing side reactions between the electrolyte and Gr, and facilitating the rapid formation of a thin, robust SEI. Regarding the second exothermic peak, electrodes with PVDF and PAN binders release substantial heat due to binder-lithium reactions between 200 and 300 °C, which are known to generate H_2. Conversely, the second exothermic peak of the cPAN-based lithiated Gr is minimal and even smaller than the heat released during SEI decomposition. Although all three binders contain hydrogen atoms in their molecular structures, the negligible second exothermic peak indicates that the reactivity of hydrogen atoms in cPAN is substantially lower than those in the other two binders. The minor exothermic peak may be attributed to the presence of residual branched chains in cPAN that are not fully cyclized, which can still react with lithium. Nonetheless, following dehydrogenation and cyclization heat treatment, the thermal runaway reaction between cPAN and lithium is negligible.

To explain the impact of cPAN on Gr electrodes, we discuss both the proportion and the cyclization degree of cPAN. A higher proportion of cPAN in the Gr electrode effectively suppresses electrolyte side reactions, reducing the formation of organic components in the SEI and thereby lowering the heat released during SEI decomposition (Fig. S8). However, a higher proportion of cPAN also contains more uncyclized side chains, which can react with lithium and generate additional heat. By varying the heating temperature and time, Gr electrodes using cPAN with different cyclization degrees can be obtained. Representative conditions are chosen as 260 °C for 1 h, 300 °C for 1 h, and 300 °C for 12 h to yield cPAN with different cyclization degrees. With increasing heating temperature and time, the characteristic signals of C–H bonds are weakened, confirming the decrease of active hydrogen atoms, while those of C=N and C=C bonds are intensified, indicating a higher cyclization degree (Fig. S9). In other words, the cyclization degree is positively correlated with heating temperature and time. Electrodes prepared at 260 °C for 1 h and 300 °C for 12 h, which exhibit different cyclization degrees, are selected for thermal stability comparison. The results show that lower cyclization degree leads to poorer SEI stability, resulting in greater heat released from SEI decomposition. This occurs because cPAN with low cyclization degree cannot form a uniform coating on the anode surface, weakening its suppression of side reactions and thereby reducing SEI stability. The cPAN with low cyclization degree contains more unstable side chains that readily react with lithium, generating additional heat (Fig. S10). Moreover, LIBs employing cPAN with low cyclization degree generate more H_2 (Fig. S11). Folding tests reveal that the mechanical properties of the cPAN-based electrodes improve with an increasing cyclization degree (Fig. 3(h)–S3(b), S12 and S13). These results highlight that the cyclization degree plays a decisive role in the protective function of cPAN. Insufficiently cyclized cPAN not only fails to form a thermally stable interface but also undergoes severe reactions with lithium, ultimately increasing the fraction of H_2.

To further verify the protective effect of cPAN on Gr, DSC tests are performed on mixtures of lithiated Gr and electrolyte. Since the electrolyte delays exothermic reactions, SEI decomposition peaks are nearly absent for three electrodes (Fig. 4(d)). Reactions between the lithiated Gr and electrolyte occur within the temperature range of 200–300 °C.

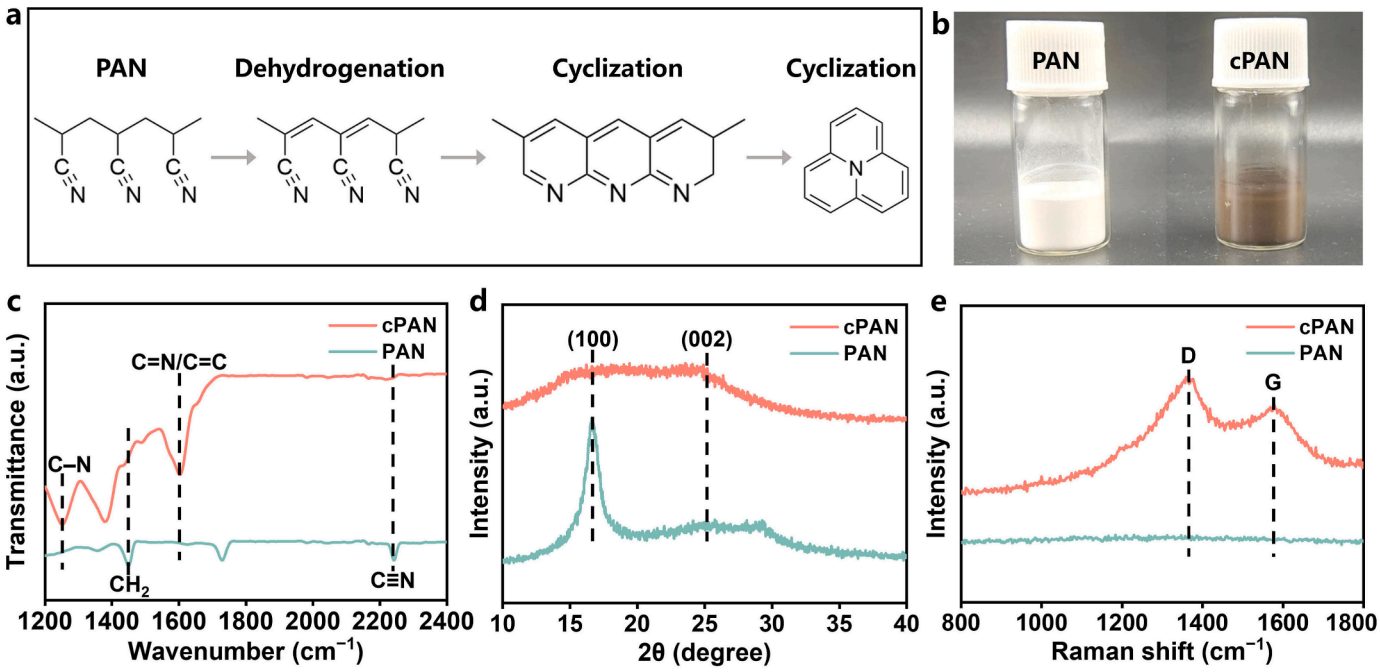

Fig. 2. Physicochemical characterization of PAN and cPAN powder. (a) Molecular structure changes during the cyclization of PAN. (b) Optical photographs, (c) FTIR spectra, (d) XRD patterns, and (e) Raman spectra of PAN and cPAN powder.

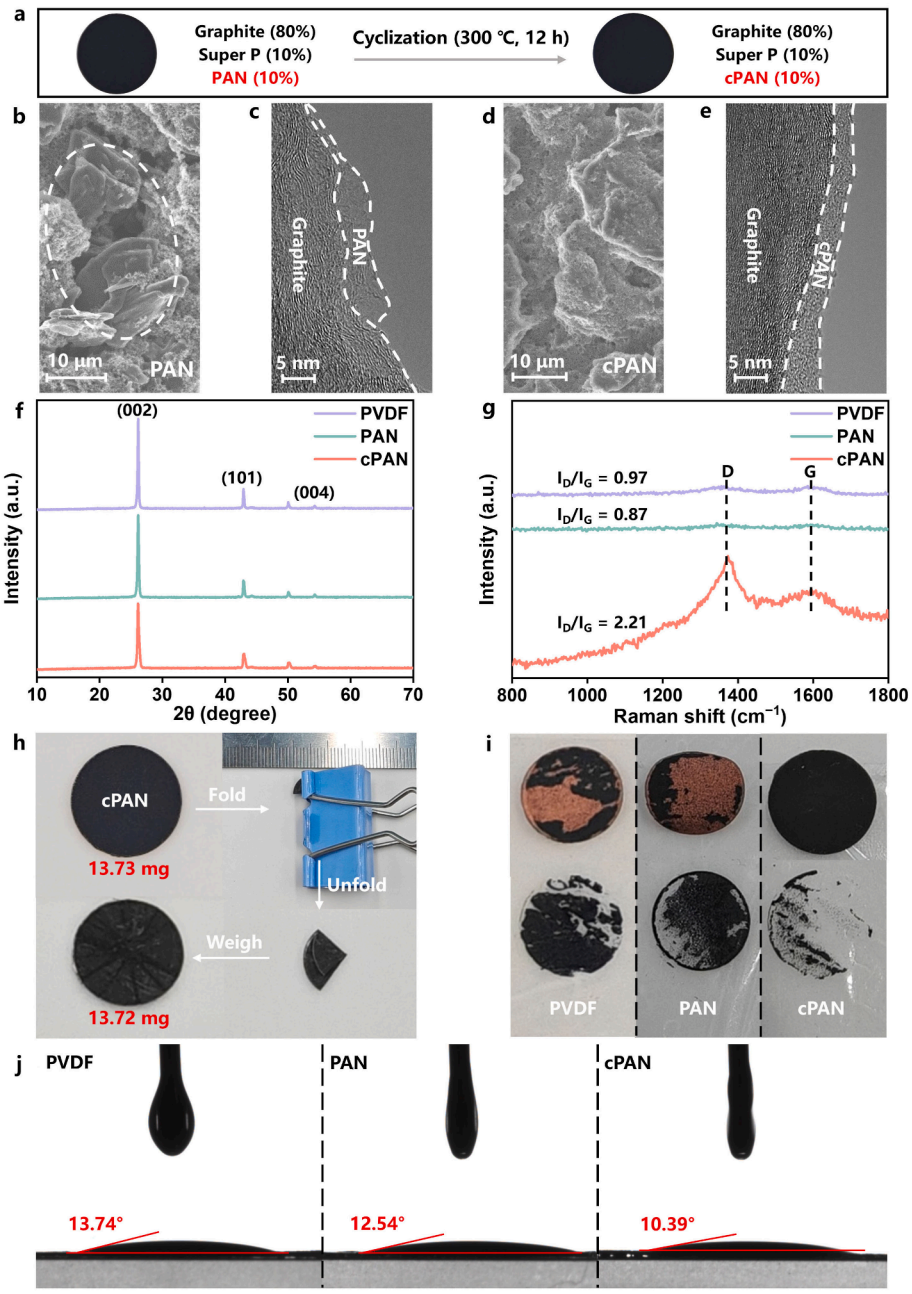

Fig. 3. Features of Gr electrodes with PVDF, PAN and cPAN binders. (a) Schematic diagram of cyclization of Gr electrodes. (b) SEM and (c) HRTEM images of Gr electrode with PAN binder before cycling. (d) SEM and (e) HRTEM images of Gr electrode with cPAN binder before cycling. (f) XRD patterns, (g) Raman spectra, (h) Folding experiments of anodes with different binders. (i) Electrodes (top) and active material on tape (bottom) after tape peeling. (j) Electrolyte wettability on the anode with different binders.

Notably, the reaction peak for the cPAN-based Gr is delayed by at least 15 °C compared to the others and is accompanied by significantly lower heat generation. These results fully demonstrate that the physical barrier formed by cPAN provides an effective protective effect in suppressing side reactions between Gr and the electrolyte. Overall, these results confirm that cPAN not only resists reactions with lithium to generate H_2 but also mitigates H_2 generation from electrolyte and hydrofluoric acid reduction. During the early and intermediate stages of thermal runaway, the electrolyte and hydrofluoric acid generate H_2 by acquiring electrons at the anode. The robust SEI promoted by cPAN exhibits excellent thermal stability, effectively preventing these species from gaining electrons at the anode and thereby reducing H_2 generation. In the late stage of thermal runaway, cPAN inherently avoids reacting with lithium to generate H_2. This multi-dimensional suppression of H_2 generation significantly enhances the thermal safety of LIBs.

2.4. Electrochemical stability

The hexagonal carbon ring, piperidine ring, and pyridine nitrogen in the cPAN are the main active sites for lithium-ion storage (Zhang et al., 2021). Half-cells employing cPAN as the active material are assembled and subjected to charge-discharge and cyclic voltammetry (CV) tests. Lithium-ion insertion and extraction are observed for cPAN electrode (Fig. S14). The first-cycle CV curve of the half-cell exhibits distinct lithium (de)intercalation peaks around 0.01 V (Fig. S15). Both the charge-discharge and CV results are in agreement with previous studies (Zhang et al., 2021), confirming that cPAN indeed serves as an effective lithium-ion storage material. When Gr electrodes are fabricated using cPAN as the binder, both Gr and cPAN contribute to the overall capacity. Comparative analysis of Gr electrodes with different cPAN binder contents reveals that the total electrode capacity depends on the proportions and specific capacities of Gr and cPAN (Fig. 5(b) and S16). In other words, the total capacity of the electrode is originated from the specific

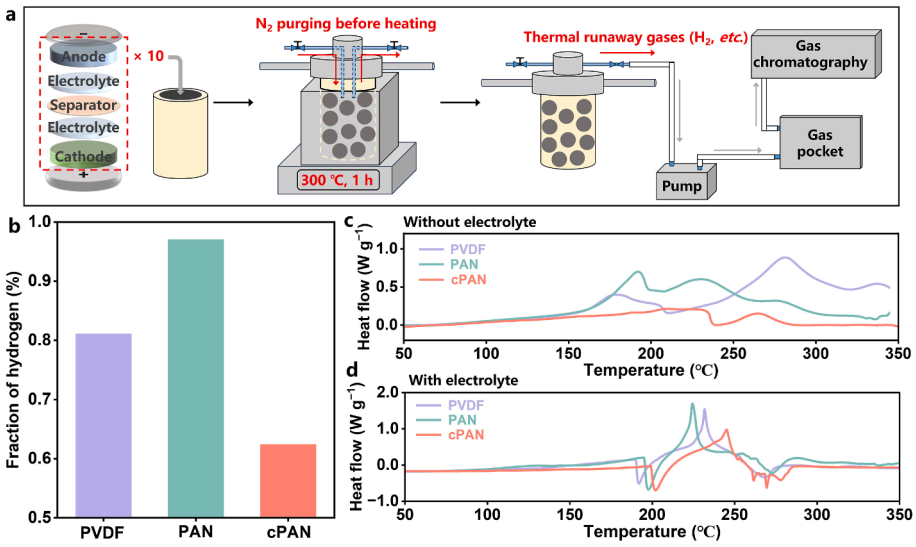

Fig. 4. Thermal characterization of Gr electrodes with PVDF, PAN and cPAN binders. (a) Scheme for testing the fraction of H_2 generated during thermal runaway. (b) Fraction of H_2 generated in (a). (c) DSC curves of lithiated Gr electrodes. (d) DSC curves of the mixture of lithiated Gr electrodes and electrolyte.

capacities of Gr and cPAN, determined by their respective mass ratios. Moreover, a higher cyclization degree generates a greater number of active sites for lithium-ion storage, consequently enhancing the overall capacity of the electrode (Fig. S17). The electrodes using cPAN treated at 300 °C for 12 and 14 h deliver comparable capacities, indicating that the optimal cyclization degree has already been achieved within 12 h.

To investigate the influence of cPAN on the electrochemical performance of LIBs, three types of Gr electrodes are assembled into both half-cells and full-cells. First, Gr/Li half-cells are evaluated at various rates to probe their kinetic behavior (Fig. 5(a)). It is evident that cPAN enhances both the capacity and rate capability of the LIBs: the specific capacity reaches 410 mAh g^{-1} at 0.1 C (1 C = 340 mA g^{-1}), 399 mAh g^{-1} at 0.2 C, 366 mAh g^{-1}at 0.5 C and 282 mAh g^{-1} at 1 C. With a Gr loading of 6 mg cm^{-2}, long-term cycling stability is assessed at 0.5 C (Fig. 5(b) and S18). The cPAN-based LIBs possess an initial specific capacity of 370 mAh g^{-1} and retain 97% of this capacity after 200 cycles, whereas LIBs using PVDF and PAN binders demonstrate lower capacities and inferior cycling stability. Even when the cPAN content is reduced from 10% to 2%, the half-cell still exhibits stable cycling performance (Fig. S19). These results demonstrate that cPAN uniformly coated on Gr significantly improves capacity, rate performance, and long-term stability. Subsequently, LFP/Gr full-cells are assembled to further validate the advantages of cPAN. From rate capability tests, the cPAN-based full-cells outperform their counterparts: specific capacities of 155, 153, 146, 134, 121, 85, 43, and 27 mAh g^{-1} at 0.1, 0.2, 0.5, 1, 2, 5, 8, and 10 C (1 C = 150 mA g^{-1}), respectively (Fig. 5(c)). Moreover, upon returning to 0.1 C, the cPAN-based cells recover their initial capacity, indicating excellent reversibility. Long-term cycling at 0.5 C with an LFP loading of 11 mg cm^{-2} shows that the cPAN full-cells retain 72% of their initial capacity after 800 cycles, confirming their outstanding stability (Fig. 5 (d) and S20).

From these results, the uniform cPAN coating on Gr offers three key electrochemical advantages: (1) it provides additional lithium storage sites, thereby increasing the specific capacity; (2) the increased active sites and the formation of a thin and robust SEI lower both charge transfer resistance and interfacial resistance, enhancing rate capability; and (3) it mitigates side reactions between electrolyte and lithiation Gr, improving cycling stability.

To further elucidate the electrochemical properties of the Gr electrodes, CV measurements are conducted (Fig. 5(e–g)). All three electrodes exhibit consistent oxidation and reduction peaks, indicating that thermal treatment does not alter the electrochemical behavior of Gr. Notably, the first CV cycle of the cPAN-based electrode shows a broad peak between 0.5 and 1.0 V, attributable to SEI formation on the cPAN surface, thus confirming its active participation in the electrochemical processes (Fig. 5(g)) (Zhang et al., 2021). Compared with PAN, electrodes with cPAN binders display higher peak currents for both oxidation and reduction, signifying accelerated reaction kinetics and faster lithium-ion diffusion (Fig. 5(f and g)) (Sun et al., 2017; Yang et al., 2023). Additionally, the five CV cycles of the cPAN-based electrode overlap more precisely than those of the other electrodes, further evidencing its superior cycling stability.

To reveal the dynamic processes during charge and discharge, *in situ* electrochemical impedance spectroscopy (EIS) and distribution of relaxation times (DRT) analyses are performed (Fig. 5(h–j) and S21). In the DRT mappings, low-frequency peaks (the τ in the range of 10^{1} to 10^{-1}) correspond to charge transfer resistance (R_{ct}), mid-frequency peaks (the τ in the range of 10^{-1} to 10^{-3}) to the resistance of lithium-ion transport through the SEI (R_{SEI}), and high-frequency peaks (the τ in the range of 10^{-3} to 10^{-4}) to contact resistance (R_0) (Chen et al., 2023). The primary resistance differences among the electrodes during charge-discharge are observed in R_{SEI} and R_{ct}. cPAN effectively suppresses side reactions between electrolyte and lithiated Gr and, thanks to its network structure, ensures structural integrity of Gr, yielding a robust and stable SEI that minimizes R_{SEI}. The presence of cPAN increases lithium-ion storage active sites, resulting in a reduced R_{ct} (Fig. S22). In addition, after chronic thermal stress, the impedance of the cPAN-based battery shows no significant variation, demonstrating its excellent stability (Fig. S23).

2.5. *Electrode–electrolyte interphase of Gr electrodes*

To investigate the protective role of cPAN on Gr during cycling, X-ray photoelectron spectroscopy (XPS) is employed to characterize Gr electrodes after 200 charge-discharge cycles. The changes in the SEI are analyzed based on the elemental spectra of Li, F, C, and O. The Li 1s XPS spectra reveal that the SEI of three types of Gr electrodes contains $ROCO_2Li$, Li_2CO_3, and LiF (Fig. 6(a)) (Hong et al., 2025; Suh et al., 2025; Yang et al., 2022). A substantial amount of organic components ($ROCO_2Li$) is detected in the SEI formed on electrodes using PVDF and PAN as binders, indicating poor interfacial stability during cycling. This instability leads to repetitive rupture and reformation of the SEI, resulting in continuous thickening of the interphase and sustained electrolyte consumption. In contrast, the SEI formed on the cPAN-based

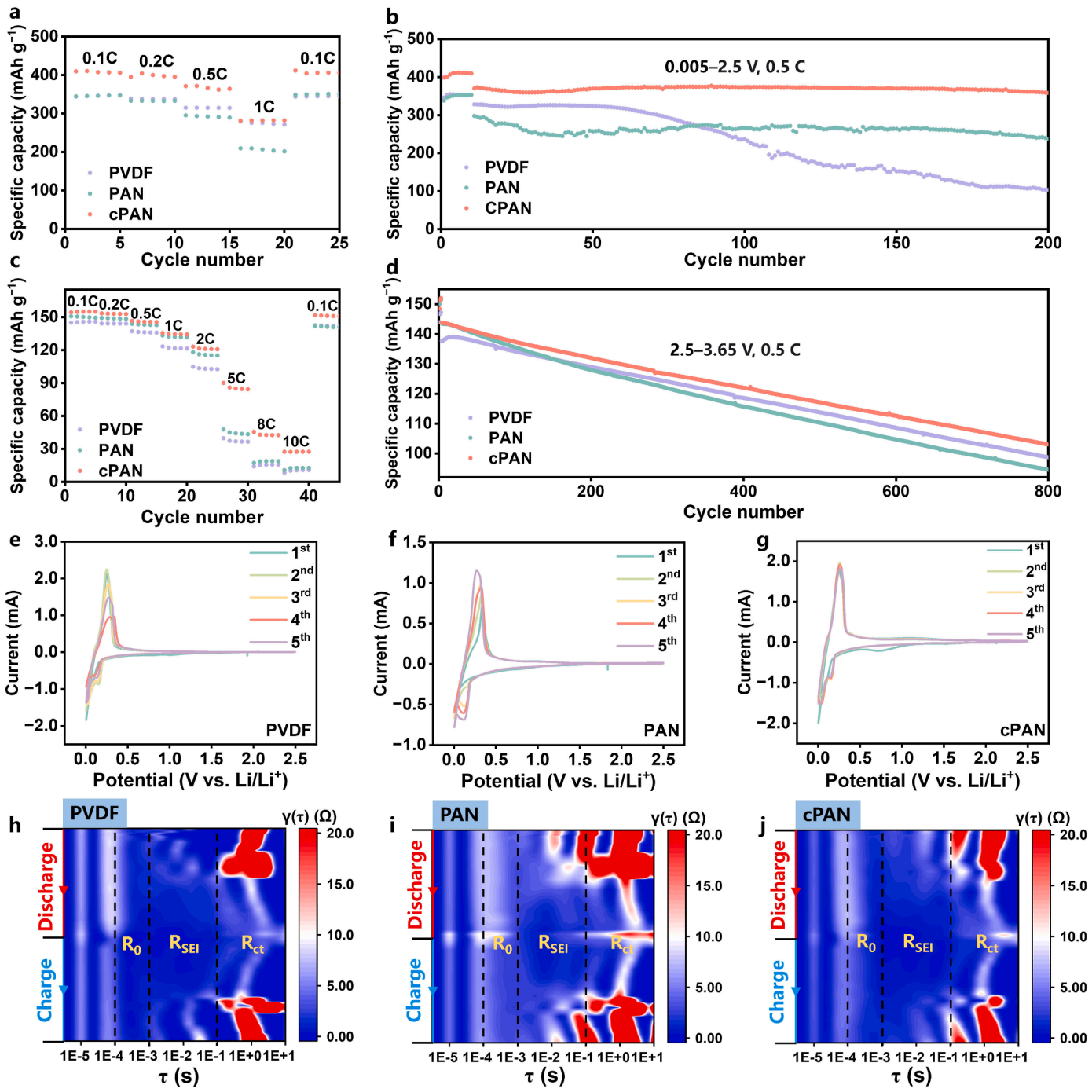

Fig. 5. Electrochemical characterization of Gr electrodes with PVDF, PAN and cPAN binders. (a) Rate performance of Gr/Li half-cells. (b) Long-term cycling performance of Gr/Li half-cells. (c) Rate performance of LFP/Gr full-cells. (d) Long-term cycling performance of LFP/Gr full-cells. (e−g) CV curves of Gr/Li half-cells at 0.1 mV s^{-1} (h−j) *In-situ* DRT mappings of Gr/Li half-cells.

electrode is predominantly composed of inorganic species (Li_2CO_3 and LiF) (Fig. 6(b)). This suggests that cPAN effectively suppresses side reactions between the electrolyte and lithiated Gr, thereby facilitating the formation of a thin and robust SEI. The O 1s XPS spectra further confirm that the SEI on the cPAN-based Gr electrode contains the lowest amount of organic species (Fig. S24). Additionally, the F 1s spectra show the presence of P–F and Li–F species in the SEI of electrodes using PAN and cPAN binders, attributed to the decomposition of the electrolyte. Notably, in the case of the PVDF-based electrode, a distinctive C–F signal is observed in the F 1s spectra, originating from the PVDF binder itself (Fig. 6(c)) (Liao et al., 2025; Yu et al., 2022). This C–F signal is also evident in the C 1s spectra (Fig. S25), indicating binder degradation and active material detachment during cycling. These results demonstrate the inferior cycling stability of PVDF-based electrodes. Moreover, the F 1s spectra verify that the cPAN-based electrodes possess the highest proportion of inorganic species, corroborating the aforementioned observations (Fig. 6(d)).

To further analyze the internal composition of the SEI, sputtering is conducted on the SEI of the three electrodes, with each sputtering depth set at 20 nm (Fig. S26). For the PVDF- and PAN-based electrodes, the ratio of F atoms in the SEI remains below 10% and exhibits an overall decreasing trend, indicating a low proportion of inorganic components.

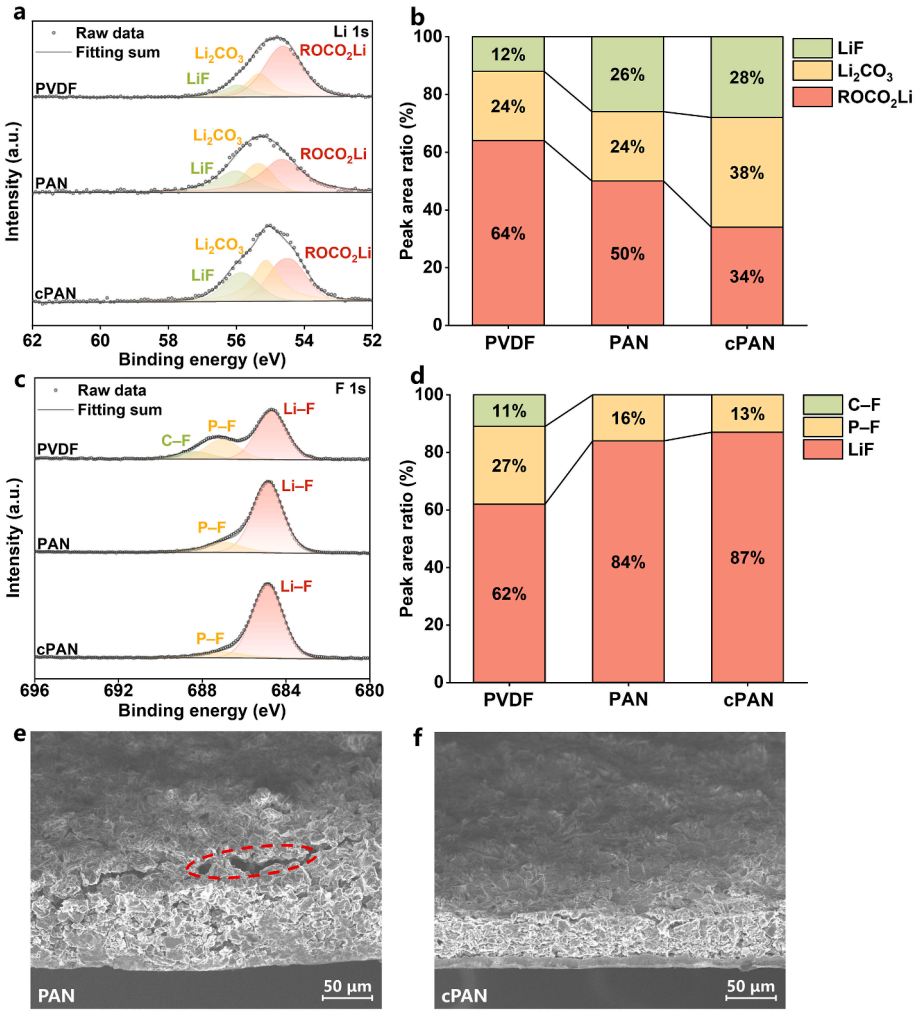

Fig. 6. Electrochemical characterization of cycled Gr anode. (a–d) XPS spectra of Li 1s and F 1s for SEI of Gr electrodes with PVDF, PAN and cPAN as binders. (e and f) SEM images of Gr electrodes with PAN and cPAN as binders after 200 cycles.

In contrast, the SEI of the cPAN-based electrode consistently maintains an F atomic ratio above 20%, which further increases with sputtering depth. This result demonstrates that both the surface and interior of the SEI are enriched in inorganic components, suggesting that cPAN effectively mitigates electrolyte side reactions and enhances cycling stability.

To further elucidate the protective effect of cPAN, the cross-sections of Gr electrodes after 200 cycles are examined via SEM. The electrode using PAN as the binder exhibits visible surface cracks, indicating structural degradation due to poor cycling stability (Fig. 6(e)). In stark contrast, the cPAN-based electrode maintains a smooth and intact surface morphology after cycling (Fig. 6(f)). After chronic thermal stress, the cPAN-based electrode still remains flat (Fig. S27). These results clearly demonstrate that electrodes using PVDF and PAN as binders suffer from unstable electrode–electrolyte interphases, leading to active material detachment and structural damage. In comparison, cPAN significantly enhances the interfacial stability, enabling the Gr electrode to maintain long-term structural integrity and cycling stability.

3. Conclusion

This study proposes a direct heating approach of anodes to achieve *in situ* cPAN in Gr, simultaneously enhancing both the thermal safety and electrochemical performance of LIBs. Specifically, during thermal runaway, cPAN possesses excellent thermal stability and does not react with lithium, effectively suppressing H_2 generation. Moreover, cPAN inhibits side reactions between the electrolyte and lithiated Gr, reducing H_2 generation caused by electrolyte and hydrofluoric acid reduction at the anode. These results indicate that cPAN mitigates H_2 generation from multiple pathways during thermal runaway, resulting in a reduction of hydrogen fraction by more than 23%. Meanwhile, cPAN increases the peak SEI decomposition temperature to above 200 °C and delays the peak reaction temperature between lithiated Gr and the electrolyte by at least 15 °C, while significantly reducing the heat released from these exothermic processes. Electrochemically, cPAN serves as a lithium-ion storage active material, significantly increasing the specific capacity of Gr electrodes, achieving up to 410 mAh g^{-1} at 0.1 C. The increasing lithium storage sites decreases charge transfer resistance, while cPAN also promotes the formation of a thin, robust SEI, reducing interfacial resistance. The resistance reduction translates to outstanding rate capability for LIBs employing cPAN as the binder, particularly in full-cell. Furthermore, cPAN suppresses side reactions between electrolyte and lithiated Gr, enhancing cycling stability, with capacity retention of 97% after 200 cycles in half-cells and 72% after 800 cycles in full-cells. The simultaneous improvements in thermal safety and electrochemical performance can be attributed to the facilitation of a stable electrode–electrolyte interphase. Owing to its advantages in thermal safety, mechanical property and electrochemical performance, cPAN is expected to be extensively investigated and applied in hard carbon, silicon and other advanced battery systems. This work provides valuable insights toward the design of LIBs that meet stringent requirements for

both high safety and high performance. Currently, validations in large-capacity batteries are restricted by current fabrication techniques and the stringent safety protocols required for handling large volumes of explosive gases. In industrial production, numerous large-format electrodes can be simultaneously processed in advanced thermal treatment systems. This significantly reduces the average cost and energy consumption, facilitating the fabrication of large-scale batteries.

CRediT authorship contribution statement

Kai Chen: Writing – original draft, Formal analysis, Data curation, Conceptualization. **Dian Zhang:** Data curation, Conceptualization. **Feng Jiang:** Formal analysis, Data curation. **Nai-Lu Shen:** Formal analysis, Data curation. **Xiao-Hui Yan:** Formal analysis, Data curation. **Ke-Feng Ren:** Formal analysis, Data curation. **Xin Shen:** Methodology, Investigation. **Lungang Chen:** Resources, Methodology. **He Liu:** Resources, Methodology. **Faxing Wang:** Validation, Supervision. **Shengjie Peng:** Methodology, Investigation. **Yuping Wu:** Visualization, Validation. **Xin-Bing Cheng:** Writing – review & editing, Validation, Resources, Methodology, Investigation, Funding acquisition.

Declaration of competing interest

The authors declare that they have no known competing financial interests or personal relationships that could have appeared to influence the work reported in this paper.

Acknowledgements

This work was supported by the National Natural Science Foundation of China (Grant Nos. 92372111 and 22179070), the Fundamental Research Funds for the Central Universities (Grant No. RF1028623157). The authors appreciate the Scientific Compass (https://www.shiyanjia.com) for FTIR tests. The authors acknowledge the Jushang Scientific Research Service Platform (www.jsceshi.cn) for providing SEM measurement. The authors appreciate eceshi (www.eceshi.com) for the XPS analysis.

Appendix A. Supplementary data

Supplementary data to this article can be found online at https://doi.org/10.1016/j.partic.2026.05.005.

References

Agostini, M., Brutti, S., & Hassoun, J. (2016). High voltage Li-ion battery using exfoliated graphite/graphene nanosheets anode. *ACS Applied Materials and Interfaces, 8*(17), 10850–10857. https://doi.org/10.1021/acsami.6b01407

Bashir, T., Wu, T., Zhang, J.-H., Hu, R.-J., Li, Q.-G., Song, Y.-Z., & Kong, L. (2025). Tuning and understanding the solvation structure with salt concentrations for stable dual ion batteries. *Chinese Chemical Letters.* , Article 112091. https://doi.org/10.1016/j.cclet.2025.112091

Chen, Y., He, Q., Zhao, Y., Zhou, W., Xiao, P., Gao, P., et al. (2023). Breaking solvation dominance of ethylene carbonate via molecular charge engineering enables lower temperature battery. *Nature Communications, 14*(1), Article 8326. https://doi.org/10.1038/s41467-023-43163-9

Chen, H., Wu, T., Zhang, J., Fan, X., Ju, W., Chen, J., et al. (2026). Anion coordination strength mediated aluminum corrosion for high-voltage lithium-metal batteries. *Particuology, 111*, 50–57. https://doi.org/10.1016/j.partic.2026.01.019

Chen, J., Xu, C., Wang, Q., Wang, H., Peng, Y., Liu, J., et al. (2025). The thermal-gas coupling mechanism of lithium iron phosphate batteries during thermal runaway. *Journal of Power Sources, 625*, Article 235728. https://doi.org/10.1016/j.jpowsour.2024.235728

Chen, K., Zhang, D., Guo, J.-X., Jiang, F., Shen, N., Yan, X., et al. (2025). Hydrogen generated from binders: An overlooked thermal runaway source in lithium-ion batteries. *Journal of Energy Chemistry, 109*, 602–608. https://doi.org/10.1016/j.jechem.2025.06.004

Chiu, Y.-C., Liao, C.-P., Wang, C.-H., Pourzolfaghar, H., & Li, Y.-Y. (2025). Antisolvent spraying strategy for synthesizing spherical micro silicon-cyclized polyacrylonitrile composites to boot initial coulombic efficiency and ultra-high capacity in lithium-ion batteries. *Chemical Engineering Journal, 504*, Article 158583. https://doi.org/10.1016/j.cej.2024.158583

Ding, Y., Jiang, Y., Jin, D., Jiang, Y., & Alcântara, A. C. S. (2025). Unlocking the potential of sepiolite: Designing high-performance energy storage materials. *Energy Reviews, 4*(2), Article 100127. https://doi.org/10.1016/j.enrev.2024.100127

Feng, X., Ren, D., He, X., & Ouyang, M. (2020). Mitigating thermal runaway of lithium-ion batteries. *Joule, 4*(4), 743–770. https://doi.org/10.1016/j.joule.2020.02.010

Guerra, O. J., Zhang, J., Eichman, J., Denholm, P., Kurtz, J., & Hodge, B.-M. (2020). The value of seasonal energy storage technologies for the integration of wind and solar power. *Energy & Environmental Science, 13*(7), 1909–1922. https://doi.org/10.1039/d0ee00771d

Guo, J.-X., Gao, C., Du, Y.-F., Jiang, F., Shen, N.-L., Tang, W.-B., et al. (2025). Thermoresponsive mono-solvent electrolyte inhibiting parasitic reactions for safe lithium metal batteries. *Advanced Energy Materials, 15*, Article 2500703. https://doi.org/10.1002/aenm.202500703

Guo, J.-X., Jiang, F., Shen, N.-L., Tang, W.-B., Wang, T., Ma, Y., et al. (2024). Host-guest interactions for electrochemically stable and thermally safe lithium metal batteries. *ACS Energy Letters, 9*(10), 4800–4809. https://doi.org/10.1021/acsenergylett.4c01583

Hong, C., Tao, R., Tan, S., Pressley, L. A., Bridges, C. A., Li, H.-Y., et al. (2025). In situ cyclized polyacrylonitrile coating: Key to stabilizing porous high-entropy oxide anodes for high-performance lithium-ion batteries. *Advanced Functional Materials, 35*(2), Article 2412177. https://doi.org/10.1002/adfm.202412177

Huang, Z., Li, X., Wang, Q., Duan, Q., Li, Y., Li, L., & Wang, Q. (2021). Experimental investigation on thermal runaway propagation of large format lithium ion battery modules with two cathodes. *International Journal of Heat and Mass Transfer, 172*, Article 121077. https://doi.org/10.1016/j.ijheatmasstransfer.2021.121077

Jia, Z., Qin, P., Li, Z., Wei, Z., Jin, K., Jiang, L., & Wang, Q. (2022). Analysis of gas release during the process of thermal runaway of lithium-ion batteries with three different cathode materials. *Journal of Energy Storage, 50*, Article 104302. https://doi.org/10.1016/j.est.2022.104302

Jiang, F., Du, Y.-F., Guo, J.-X., Shen, N.-L., Chen, Z.-X., Geng, M., et al. (2025). Thermoresponsive solid electrolyte interphase enables safe lithium-sulfur batteries with high energy density. *Energy & Environmental Science, 18*(10), 4925–4933. https://doi.org/10.1039/d5ee00412h

Jiang, Z.-J., Luo, Z.-H., Guo, J.-X., Du, Y.-F., Jiang, F., Shen, N.-L., et al. (2025). Thermal safety overview of silicon-carbon anode in lithium-ion batteries: Key parameters in determining the reactivity. *Particuology, 100*, 178–185. https://doi.org/10.1016/j.partic.2025.03.013

Jiang, Y., Sun, C., Dong, F., Xie, H., & Sun, L. (2024). Multilayer polyethylene separator with enhanced thermal properties for safe lithium-ion batteries. *Particuology, 91*, 29–37. https://doi.org/10.1016/j.partic.2023.12.017

Jiang, Y., Wen, S., Lin, S., Jin, D., & Ding, Y. (2024). Influence of sepiolite on the rheological properties of PVA composite hydrogels. *ChemistrySelect, 9*(24), Article e202401210. https://doi.org/10.1002/slct.202401210

Jiang, F.-N., Yang, S.-J., Chen, Z.-X., Liu, H., Yuan, H., Liu, L., et al. (2023). Higher-order polysulfides induced thermal runaway for 1.0 Ah lithium sulfur pouch cells. *Particuology, 79*, 10–17. https://doi.org/10.1016/j.partic.2022.11.009

Kim, K., Ma, H., Park, S., & Choi, N.-S. (2020). Electrolyte-additive-driven interfacial engineering for high-capacity electrodes in lithium-ion batteries: Promise and challenges. *ACS Energy Letters, 5*(5), 1537–1553. https://doi.org/10.1021/acsenergylett.0c00468

Lavi, O., Haik, O., Hirshberg, D., Talyosef, Y., Zinigard, E., Markovsky, B., et al. (2019). Abnormal electrochemical behavior of rounded graphite. *Carbon, 154*, 313–321. https://doi.org/10.1016/j.carbon.2019.07.080

Lei, S., Sun, W., & Yang, Y. (2024). Comprehensive technology for recycling and regenerating materials from spent lithium iron phosphate battery. *Environmental Science and Technology, 58*(8), 3609–3628. https://doi.org/10.1021/acs.est.3c08585

Liao, K., Pai, M.-H., & Manthiram, A. (2025). Tuning the solvation structure of a weakly solvating cyclic ether electrolyte for wide-temperature cycling of lithium-sulfurized polyacrylonitrile batteries. *Advanced Energy Materials, 15*(10), Article 2403733. https://doi.org/10.1002/aenm.202403733

Liu, X., Yin, L., Ren, D., Wang, L., Ren, Y., Xu, W., et al. (2021). In situ observation of thermal-driven degradation and safety concerns of lithiated graphite anode. *Nature Communications, 12*(1), Article 4235. https://doi.org/10.1038/s41467-021-24404-1

Luo, Y.-H., Pan, Q.-L., Wei, H.-X., Huang, Y.-D., Li, P.-Y., Tang, L.-B., et al. (2024). Revealing proton-coupled exchange mechanism in aqueous ion-exchange synthesis of nickel-rich layered cathodes for lithium-ion batteries. *eScience, 4*(4), Article 100229. https://doi.org/10.1016/j.esci.2024.100229

Luo, Z.-H., Zhang, D., Guo, J.-X., Jiang, F., Shen, N.-L., Du, Y.-F., et al. (2025). Recent progress on the materials design towards thermally safe sodium-ion batteries. *Journal of Energy Chemistry, 102*, 555–575. https://doi.org/10.1016/j.jechem.2024.11.014

Meng, N., Zhu, X., & Lian, F. (2022). Particles in composite polymer electrolyte for solid-state lithium batteries: A review. *Particuology, 60*, 14–36. https://doi.org/10.1016/j.partic.2021.04.002

Metzger, M., Strehle, B., Solchenbach, S., & Gasteiger, H. A. (2016). Origin of H_2 evolution in LIBs: H_2O reduction vs. electrolyte oxidation. *Journal of the Electrochemical Society, 163*(5), A798–A809. https://doi.org/10.1149/2.1151605jes

Piper, D. M., Yersak, T. A., Son, S.-B., Kim, S. C., Kang, C. S., Oh, K. H., et al. (2013). Conformal coatings of cyclized-PAN for mechanically resilient Si nano-composite anodes. *Advanced Energy Materials, 3*(6), 697–702. https://doi.org/10.1002/aenm.201200850

Qin, T., Yang, H., Li, Q., Yu, X., & Li, H. (2024). Design of functional binders for high-specific-energy lithium-ion batteries: From molecular structure to electrode properties. *Industrial Chemistry & Materials, 2*(2), 191–225. https://doi.org/10.1039/d3im00089c

Ren, D., Feng, X., Liu, L., Hsu, H., Lu, L., Wang, L., et al. (2021). Investigating the relationship between internal short circuit and thermal runaway of lithium-ion batteries under thermal abuse condition. *Energy Storage Materials, 34*, 563–573. https://doi.org/10.1016/j.ensm.2020.10.020

Seong, W. M., Park, K.-Y., Lee, M. H., Moon, S., Oh, K., Park, H., et al. (2018). Abnormal self-discharge in lithium-ion batteries. *Energy & Environmental Science, 11*(4), 970–978. https://doi.org/10.1039/c8ee00186c

Shen, H., Wang, H., Li, M., Li, C., Zhang, Y., Li, Y., et al. (2023). Thermal runaway characteristics and gas composition analysis of lithium-ion batteries with different LFP and NCM cathode materials under inert atmosphere. *Electronics, 12*(7), Article 1603. https://doi.org/10.3390/electronics12071603

Shi, Y.-Q., Wu, T., Zhang, J.-h., Song, L., Chen, X.-D., Sun, Y.-J., et al. (2026). Tethering transition metals of Li-rich manganese oxides via anion coordination for high-voltage lithium-metal batteries. *Advanced Functional Materials, 36*(3), Article e14328. https://doi.org/10.1002/adfm.202514328

Suh, J. H., Han, S. A., Yang, S. Y., Lee, J. W., Shimada, Y., Lee, S.-M., et al. (2025). Toward fast-charging and dendritic-free Li growth on natural graphite through intercalation/conversion on MoS_2 nanosheets. *Advanced Materials, 37*(7), Article 2414117. https://doi.org/10.1002/adma.202414117

Sun, Y., Dong, H., Xu, Y., Zhang, Y., Zhao, C., Wang, D., et al. (2017). Incorporating cyclized-polyacrylonitrile with $Li_4Ti_5O_{12}$ nanosheet for high performance lithium ion battery anode material. *Electrochimica Acta, 246*, 106–114. https://doi.org/10.1016/j.electacta.2017.05.080

Sun, Q., Hu, G., Peng, Z., Cao, Y., Zhu, F., Zhang, Y., et al. (2021). Achieving a bifunctional conformal coating on nickel-rich cathode $LiNi_{0.8}Co_{0.1}Mn_{0.1}O_2$ with half-cyclized polyacrylonitrile. *Electrochimica Acta, 386*, Article 138440. https://doi.org/10.1016/j.electacta.2021.138440

Wang, D., Dong, H., Zhang, H., Zhang, Y., Xu, Y., Zhao, C., et al. (2016). Enabling a high performance of mesoporous α-Fe_2O_3 anodes by building a conformal coating of cyclized-PAN network. *ACS Applied Materials and Interfaces, 8*(30), 19524–19532. https://doi.org/10.1021/acsami.6b06096

Wang, M., Liu, K., Dutta, S., Alessi, D. S., Rinklebe, J., Ok, Y. S., & Tsang, D. C. W. (2022). Recycling of lithium iron phosphate batteries: Status, technologies, challenges, and prospects. *Renewable & Sustainable Energy Reviews, 163*, Article 112515. https://doi.org/10.1016/j.rser.2022.112515

Wang, H., Xu, H., Zhang, Z., Wang, Q., Jin, C., Wu, C., et al. (2022). Fire and explosion characteristics of vent gas from lithium-ion batteries after thermal runaway: A comparative study. *eTransportation, 13*, Article 100190. https://doi.org/10.1016/j.etran.2022.100190

Wang, Z., Yuan, J., Zhu, X., Wang, H., Huang, L., Wang, Y., & Xu, S. (2021). Overcharge-to-thermal-runaway behavior and safety assessment of commercial lithium-ion cells with different cathode materials: A comparison study. *Journal of Energy Chemistry, 55*, 484–498. https://doi.org/10.1016/j.jechem.2020.07.028

Wei, G., Huang, R., Zhang, G., Jiang, B., Zhu, J., Guo, Y., et al. (2023). A comprehensive insight into the thermal runaway issues in the view of lithium-ion battery intrinsic safety performance and venting gas explosion hazards. *Applied Energy, 349*, Article 121651. https://doi.org/10.1016/j.apenergy.2023.121651

Xu, A., Jin, Z., Wang, B., Xie, X., Xiao, X., Wang, A., et al. (2024). Unraveling the mechanism on improved kinetics performance of sulfurized polyacrylonitrile with defective conductive carbon matrix. *Chemical Engineering Journal, 484*, Article 149558. https://doi.org/10.1016/j.cej.2024.149558

Yang, S.-J., Hu, J.-K., Jiang, F.-N., Cheng, X.-B., Sun, S., Hsu, H.-J., et al. (2023). Oxygen-induced thermal runaway mechanisms of Ah-level solid-state lithium metal pouch cells. *eTransportation, 18*, Article 100279. https://doi.org/10.1016/j.etran.2023.100279

Yang, X.-G., Liu, T., & Wang, C.-Y. (2021). Thermally modulated lithium iron phosphate batteries for mass-market electric vehicles. *Nature Energy, 6*(2), 176–185. https://doi.org/10.1038/s41560-020-00757-7

Yang, S.-J., Yao, N., Jiang, F.-N., Xie, J., Sun, S.-Y., Chen, X., et al. (2022). Thermally stable polymer-rich solid electrolyte interphase for safe lithium metal pouch cells. *Angewandte Chemie International Edition, 61*(51), Article e202214545. https://doi.org/10.1002/anie.202214545

Yu, J. H., Köster, K., Voronina, N., Kim, S., Shin, H.-J., Kim, K. S., et al. (2025). Elevating Li-ion battery paradigms: Sophisticated ionic architectures in lithium-excess layered oxides for unprecedented electrochemical performance. *eScience, 5*(4), Article 100376. https://doi.org/10.1016/j.esci.2025.100376

Yu, W., Yu, Z., Cui, Y., & Bao, Z. (2022). Degradation and speciation of Li salts during XPS analysis for battery research. *ACS Energy Letters, 7*(10), 3270–3275. https://doi.org/10.1021/acsenergylett.2c01587

Zantye, M. S., Gandhi, A., Wang, Y., Vudata, S. P., Bhattacharyya, D., & Hasan, M. M. F. (2022). Optimal design and integration of decentralized electrochemical energy storage with renewables and fossil plants. *Energy & Environmental Science, 15*(10), 4119–4136. https://doi.org/10.1039/d2ee00771a

Zhang, Y., Cheng, S., Mei, W., Jiang, L., Jia, Z., Cheng, Z., et al. (2023). Understanding of thermal runaway mechanism of $LiFePO_4$ battery in-depth by three-level analysis. *Applied Energy, 336*, Article 120695. https://doi.org/10.1016/j.apenergy.2023.120695

Zhang, X., Li, L., Fan, E., Xue, Q., Bian, Y., Wu, F., & Chen, R. (2018). Toward sustainable and systematic recycling of spent rechargeable batteries. *Chemical Society Reviews, 47*(19), 7239–7302. https://doi.org/10.1039/c8cs00297e

Zhang, H., Peng, Y., Hu, Y., Pan, S., Tang, S., Luo, Y., et al. (2025). Quantitative analysis of aging and rollover failure mechanisms of lithium-ion batteries at accelerated aging conditions. *Advanced Energy Materials, 15*(19), Article 2404997. https://doi.org/10.1002/aenm.202404997

Zhang, H., Quan, L., Shi, F., Li, C., Liu, H., & Xu, L. (2018). Rheological behavior of amino-functionalized multi-walled carbon nanotube/polyacrylonitrile concentrated solutions and crystal structure of composite fibers. *Polymers, 10*(2), 186. https://doi.org/10.3390/polym10020186. Article 186.

Zhang, W., Sun, M., Yin, J., Abou-Hamad, E., Schwingenschlogl, U., Costa, P. M. F. J., & Alshareef, H. N. (2021). A cyclized polyacrylonitrile anode for alkali metal ion batteries. *Angewandte Chemie International Edition, 60*(3), 1355–1363. https://doi.org/10.1002/anie.202011484

Zhang, J.-H., Zhang, Y., Gu, Z.-Y., Chen, J.-X., Yu, C.-H., Belgibayeva, A., et al. (2026). Dampening lithium charge density by clustering solvents and anions to tame lithium de-coordination energy for low-temperature lithium-metal batteries. *Advanced Energy Materials, 16*(13), Article e05551. https://doi.org/10.1002/aenm.202505551

Zhao, L., Hou, J., Feng, X., Xu, J., Xu, C., Wang, H., et al. (2024). The trade-off characteristic between battery thermal runaway and combustion. *Energy Storage Materials, 69*, Article 103380. https://doi.org/10.1016/j.ensm.2024.103380

Zheng, Y., Shi, Z., Ren, D., Chen, J., Liu, X., Feng, X., et al. (2022). In-depth investigation of the exothermic reactions between lithiated graphite and electrolyte in lithium-ion battery. *Journal of Energy Chemistry, 69*, 593–600. https://doi.org/10.1016/j.jechem.2022.01.027